



Heterojunction of facet coupled g-C₃N₄/surface-fluorinated TiO₂ nanosheets for organic pollutants degradation under visible LED light irradiation

Kai Dai^a, Luhua Lu^{b,*}, Changhao Liang^c, Qi Liu^d, Guangping Zhu^a

^a College of Physics and Electronic Information, Huaibei Normal University, Huaibei 235000, People's Republic of China

^b State Key Lab of Advanced Technology for Materials Synthesis and Processing, Wuhan University of Technology, Wuhan 430070, People's Republic of China

^c Key Laboratory of Materials Physics and Anhui Key Laboratory of Nanomaterials and Nanotechnology, Institute of Solid State Physics, Hefei Institutes of Physical Science, Chinese Academy of Sciences, Hefei 23003, People's Republic of China

^d Laboratory of Nano-Fabrication and Novel Devices Integrated Technology, Institute of Microelectronics, Chinese Academy of Sciences, Beijing 100029, People's Republic of China

ARTICLE INFO

Article history:

Received 16 January 2014

Received in revised form 17 March 2014

Accepted 19 March 2014

Available online 27 March 2014

Keywords:

C₃N₄

F-TiO₂ nanosheets

Facet

Hybrid

Photocatalytic activity

ABSTRACT

Novel construction of a heterojunction structure by facet coupling of surface-fluorinated TiO₂ (F-TiO₂) nanosheet onto g-C₃N₄ nanosheet as a visible light photocatalyst was achieved through a simple hydrothermal method. Facet coupled structure between F-TiO₂-{001} nanosheet and g-C₃N₄-{002} nanosheet was evidently investigated by scanning electron microscopy (SEM), transmission electron microscopy (TEM), X-ray diffraction (XRD), X-ray photoelectron spectra (XPS), Fourier transform infrared (FT-IR) spectroscopy and UV–vis diffuse reflectance spectroscopy (DRS). The g-C₃N₄/F-TiO₂ facet coupled hybrid with remarkably increased interfacial area presented a significantly enhanced photocatalytic performance in degrading methylene blue (MB) under 410 nm LED light irradiation. The obviously reduced electron–hole recombination rate of hybrid was demonstrated from photoluminescence (PL) spectroscopy measurements and the photoelectrochemical evaluation. An optimal g-C₃N₄ content has been determined to be 30 wt%, corresponding to apparent pseudo-first-order rate constant k_{app} of 0.0374 min^{−1}. It is 4.5 times and 13.9 times more than that of pure F-TiO₂ nanosheets and commercial P25 photocatalyst, respectively.

© 2014 Elsevier B.V. All rights reserved.

1. Introduction

Semiconducting nanostructure materials have attracted widespread attentions as promising photocatalysts for their high degradation performance of organic pollutants in water and air [1–4]. High photocatalytic efficiency and good stability are the key factors affecting the practical applications of photocatalysts [5–7]. Nanostructured TiO₂ is the most famous photocatalyst. Although the remarkable progress has been made for the preparation of new photocatalytic materials such as AgBr, WO₃, Ag₃PO₄, BiOBr, Cu₂O [8–12], TiO₂ is still one of the superior candidate materials for solving environmental problems due to its well balance between photocatalytic activity, low cost, cyclic stability and environmental compatibility [13–15]. Of all crystal structure, anatase phase TiO₂ has shown higher photocatalytic efficiency than that of rutile and brookite phases [16,17]. The anatase TiO₂ with exposed active

{001} faces was found to be very key point to achieve high photocatalytic performance. A variety of efforts have been made on the fabrication of TiO₂ nanostructures with well exposed (001) facet [18–20].

Besides engineering crystal structure of TiO₂, compositing TiO₂ with other materials to form heterojunction structures was demonstrated to be useful in improving the photocatalytic activity of TiO₂-based materials due to the effective separation of electron–hole pairs and decrease of their recombination rate. MoS₂, WO₃, ZnO, SnS₂, SiO₂ and AgI have been composited to obtain an increased photocatalytic activity [21–26]. Today, in the field of organic photovoltaic cell, the planar heterojunction structure is most effectively in reducing the electron–hole recombination for the well conductance of electrons or holes in each continuous semiconductor phase while bulk heterojunction is most effectively in increasing the electron–hole separation for the large heterojunction area in the bulk mixture phase [27–30]. However, the structure engineering of planar heterojunction structure has rarely been reported in the field of photocatalysis.

* Corresponding authors. Fax: +86 27 87860563.

E-mail addresses: lhlu@whut.edu.cn (L. Lu), chliang@issp.ac.cn (C. Liang).

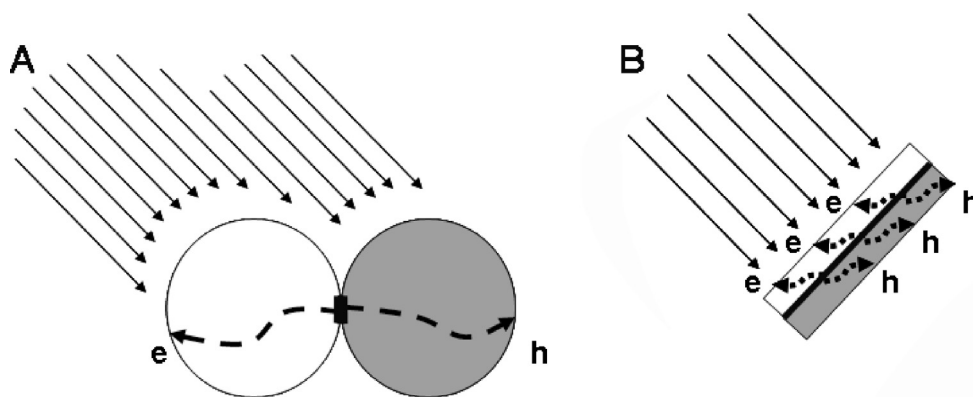


Fig. 1. The heterojunction area of (a) spherical/spherical composites and (b) nanosheet/nanosheet composites.

Inspired by this finding, we propose a novel structure of nanosheet/nanosheet semiconductor hybrids for advanced photocatalyst design. The heterojunction area within the stacked nanosheet/nanosheet should be much larger than that between quasi spherical nanoparticles and thus much higher electron–hole separation effect are expected than that of spherical/spherical heterojunction as illustrated in Fig. 1. Theoretically, the as separated electron–hole could transport to the very near reactive interface through the thin nanosheet to degrade organic pollutants. The strong energy bandgap offset within whole nanosheet of each phase within the nanosheet/nanosheet units could be helpful in reducing the recombination of electron–hole than that of spherical/spherical nanoparticle junctions.

To achieve the formation of TiO_2 -based nanosheet/nanosheet hybrid photocatalyst, surface-fluorinated TiO_2 (F- TiO_2) nanosheet with 62–71% percentage of {001} facet has been synthesized with the help of hydrogen fluoride (HF) as previous report [31]. The countering nanosheet with compatible energy band structure we chosen is graphitic carbon nitrides (g- C_3N_4), a typical metal free semiconductor that has been recognized as the most stable material with an direct band gap of 2.7 eV [32,33]. It has been considered as a “sustainable” advanced photocatalyst possessing several advantages such as visible light photocatalytic response, inexpensive, nontoxicity and stable in solutions with pH 0–14. It can be synthesized from a simple precursor via a series of polycondensation reactions [34–37]. Wang et al. firstly reported that g- C_3N_4 can be used for hydrogen and oxygen production from water splitting under visible light irradiation [38]. Yan et al. synthesized the g- C_3N_4 and applied as visible light photocatalysts to degrade methyl orange dye [39]. However, the photocatalytic

activity of pure g- C_3N_4 is very low due to the fast recombination of photo-generated electron–hole. Very recently, to improve the photocatalytic activity, the construction of heterostructures via the combination of C_3N_4 with other semiconductors, such as g- $\text{C}_3\text{N}_4/\text{ZnO}$ [40], g- $\text{C}_3\text{N}_4/\text{ZnWO}_4$ [41], $\text{AgX/g-C}_3\text{N}_4$ (X = Br, I) [42], g- $\text{C}_3\text{N}_4/\text{SmVO}_4$ [43], g- $\text{C}_3\text{N}_4/\text{Bi}_2\text{WO}_6$ [44], $\text{WO}_3/\text{g-C}_3\text{N}_4$ [45], were prepared and used for the organic dyes photodegradation. However, a well-dispersed and a large heterogeneous surface area is the most important to improve photocatalytic performance. To the best of our knowledge, there are no reports to study coupling mode of g- C_3N_4 nanosheet and anatase TiO_2 nanosheet with high couple facets composite photocatalyst. And the photocatalytic mechanism of those inorganic-organic hybrid photocatalyst remains far from clear.

In the present study, considering the possible synergic effect between F- TiO_2 nanosheet and g- C_3N_4 nanosheet, the novel facets coupling of g- C_3N_4 {002} and F- TiO_2 {001} facet hybrid was prepared by hydrothermal method without any catalysts or templates. The hybrid with optimal composition exhibits largely reduced photoluminescence (PL) intensity, indicating the remarkably depressed recombination of electrons and holes. Photoelectrochemical current is composed of un-recombined photogenerated electrons and holes. The F- TiO_2 and g- C_3N_4 hybrid with heterojunctions has shown a higher photocurrent than solely F- TiO_2 or g- C_3N_4 . In the photocatalytic experiment, the g- $\text{C}_3\text{N}_4/\text{F-TiO}_2$ hybrid has shown largely improved methylene blue (MB) photodegradation activity under visible light irradiation comparing with solely F- TiO_2 or g- C_3N_4 . An optimal degradation performance for 30%g- $\text{C}_3\text{N}_4/\text{F-TiO}_2$ was found, which shows 13.9 times catalytic activity than that of commercial Degussa P25.

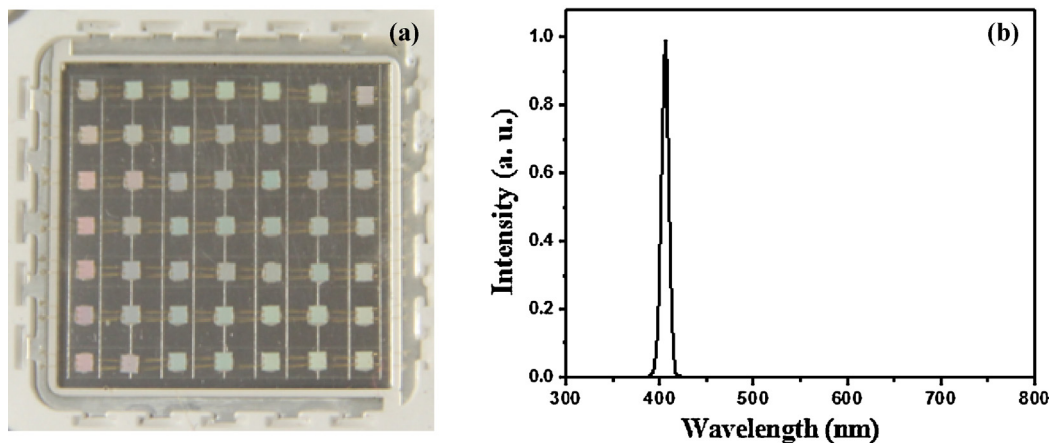


Fig. 2. (a) Photograph of LED arrays and (b) the wavelength spectrum of LED lamp.

2. Experimental

2.1. Materials

Commercial P25 TiO₂ (80% anatase and 20% rutile) was purchased from Degussa. MB, tetrabutyl titanate (Ti(OC₄H₉)₄), melamine and polyethylene glycol (PEG) were provided from Shanghai Chemical Reagent Co. Ltd., P.R. China. Sodium sulphate (Na₂SO₄) and HF were purchased from Sinopharm Chemical Reagent Co. Ltd., P.R. China. Double distilled water was used for solution preparation. All reactants were of analytical purity and used as received without any further purification.

2.2. Preparation of g-C₃N₄ nanosheet

Pure g-C₃N₄ nanosheet was synthesized by directly heating melamine. 5 g melamine powder was put into a muffle furnace and heated to 500 °C for 4 h with a heating rate of 2 °C/min. After cooling to room temperature, the raw g-C₃N₄ was obtained in a powder form.

2.3. Preparation of g-C₃N₄/F-TiO₂ hybrid

A certain of g-C₃N₄, 25 mL of Ti(OC₄H₉)₄, 3 mL HF were initially vigorously sonicated for 0.5 h to form a mixture. Then, the mixture were transferred into a 50 mL Teflon-lined autoclave and

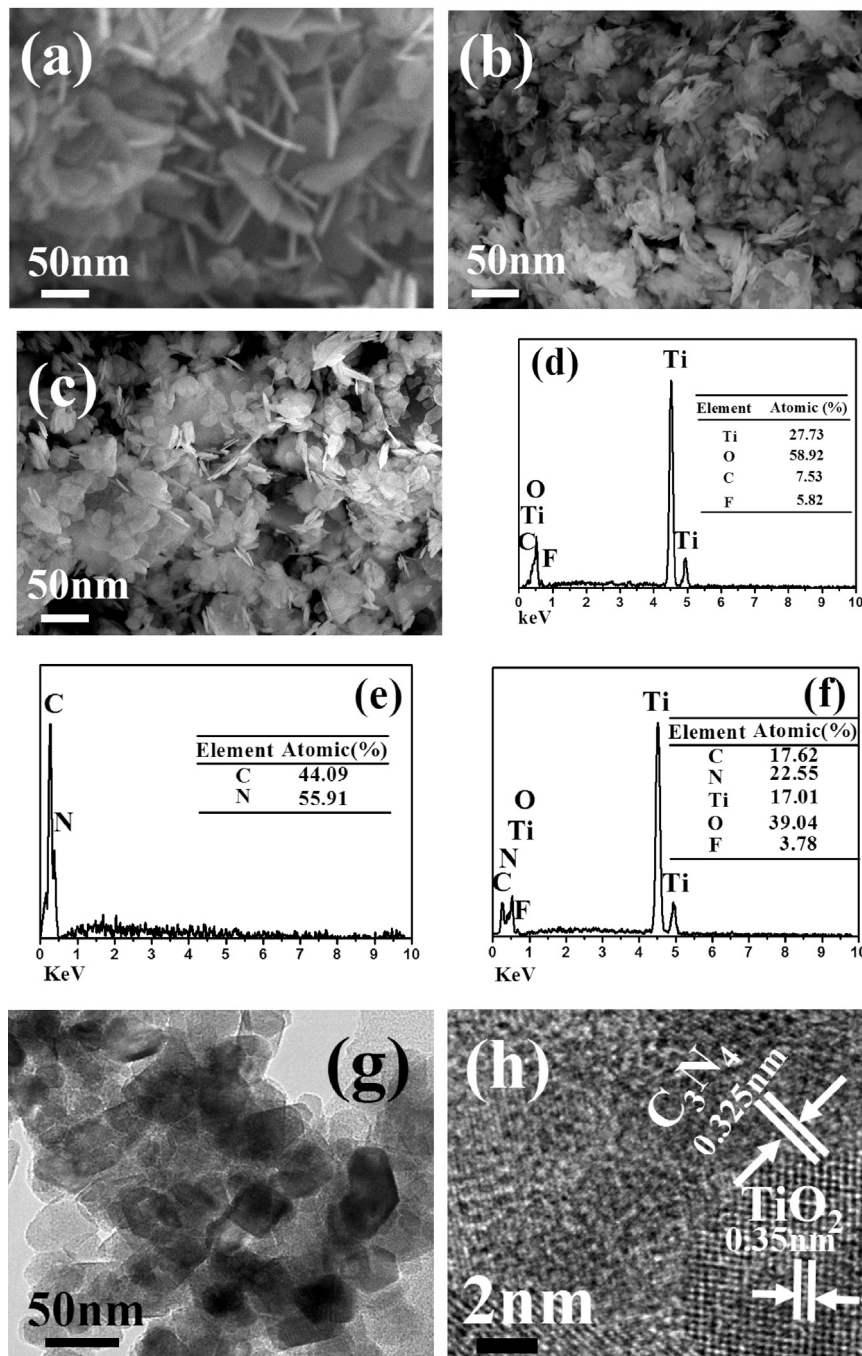


Fig. 3. SEM images of (a) F-TiO₂, (b) g-C₃N₄ and (c) 30%g-C₃N₄/F-TiO₂ hybrids, EDS spectra of (d) F-TiO₂, (e) g-C₃N₄ and (f) 30%g-C₃N₄/F-TiO₂ hybrids, TEM image of (g) 30%g-C₃N₄/F-TiO₂ hybrids and HRTEM image of (h) 30%g-C₃N₄/F-TiO₂ hybrids.

subsequently heated at 180 °C for 24 h. After hydrothermal reaction, the precipitates were harvested by centrifugation and throughout washing with water and ethanol subsequently, and then dried in an oven at 80 °C for 4 h obtaining g-C₃N₄/F-TiO₂ composites. To investigate the effect of g-C₃N₄ content on the photocatalytic performance of g-C₃N₄/F-TiO₂ hybrids, the weight percentages of g-C₃N₄ to F-TiO₂ were varied by varying the weight of g-C₃N₄, and the samples were presented as x%g-C₃N₄/TiO₂, where x is the weight content of g-C₃N₄.

2.4. Analytical and testing instruments

The structure of as-prepared sample was observed on a JEOL JEM-2010 high resolution transmission electron microscopy (HRTEM) at an accelerating voltage of 200 kV and JEOL JSM-6610LV scanning electron microscopy (SEM) with an INCA x-act energy dispersive spectrometer (EDS) at an accelerating voltage of 30 kV.

X-ray diffraction (XRD) data for different photocatalysts were measured using a Rigaku D/MAX 24000 diffractometer at room temperature with Cu K α radiation ($\lambda = 1.5406 \text{ \AA}$) in the 2θ range from 10° to 70°, operated at 40 kV and 40 mA, and a scanning speed of 8° min⁻¹.

The X-ray photoelectron spectra (XPS) of g-C₃N₄/F-TiO₂ hybrid were collected using a Thermo ESCALAB 250 with an Al K α X-ray photoelectron spectrometer at 150 W.

The infrared absorption spectra were measured by the frequency range from 400 to 4000 cm⁻¹ using a Nicolet 6700 Fourier transform infrared (FT-IR) spectra spectrophotometer. The spectra were measured after the spectrum scan of the blank pure KBr pellet.

PL spectra of g-C₃N₄-based materials were recorded by FLS920 combined fluorescence lifetime and steady state spectrometer using a 450 W Xe lamp as the excitation light source.

The wavelength of visible LED light was measured by PMS-50, current and voltage were performed by GPS-2303.

The Brunauer–Emmett–Teller (BET) specific surface area values of catalysts were measured by using nitrogen adsorption data at 77 K obtained by a Micromeritics ASAP 2010 system with multi-point BET method.

UV–vis diffuse reflectance spectroscopy (DRS) measurements were measured using a Hitachi UV-3600 UV–vis spectrophotometer equipped with an integrating sphere attachment. The analysis range was from 250 to 600 nm, and BaSO₄ was used as a reflectance standard.

The photoelectrochemical measurements were carried out on a Shanghai Chenhua CHI-660D electrochemical system, using a conventional three-electrode cell. The counter and the reference electrodes were Pt wire and saturated calomel electrode (SCE), respectively. The electrolyte solution was 1.0 M Na₂SO₄. The working electrodes were prepared as follows: 0.1 g catalyst sample was mixed with 0.02 g PEG and 0.5 mL distilled water was added to make slurry. The slurry was then injected onto a 1.0 cm \times 1.0 cm ITO glass electrode and these electrolytes were dried at 60 °C for 2 h and then calcined at 250 °C for 4 h.

2.5. Photocatalytic experiment

The photocatalytic performance of catalysts was evaluated by the photocatalytic degradation of MB under 50 W 410 nm LED light irradiation. As indicated in Fig. 2a, 7 \times 7 LED arrays were used as the light source of the photocatalytic degradation device. Fig. 2b shows the wavelength spectrum of LED at room temperature. The result showed that the emission center wavelength of LED is 410 nm with very narrow wavelength range.

The photocatalytic experiments were carried out in a reactor containing the 100 mL 10 mg/L aqueous solution of MB and 0.1 g photocatalyst. The distance between the LED light and the reactor

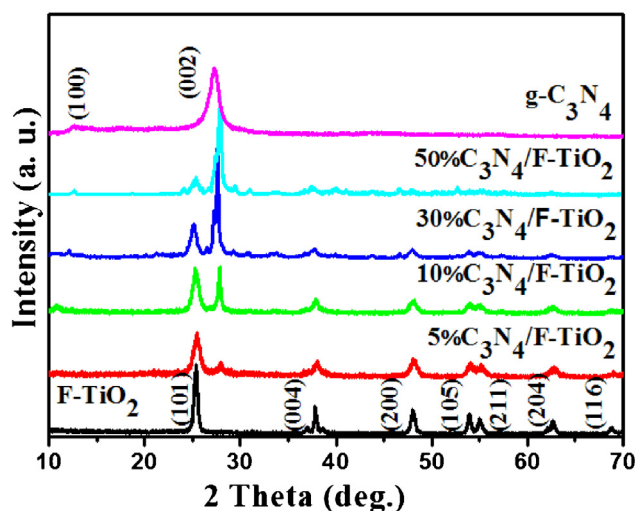


Fig. 4. XRD patterns of g-C₃N₄, F-TiO₂ and g-C₃N₄/F-TiO₂ hybrids.

was 5 cm. Then, the reactor was exposed to the LED light irradiation. At the given irradiation time, the absorbance wavelength used in the spectrophotometer analysis to determine MB concentration at 664 nm. The degradation efficiency was calculated as follows [46]:

$$\eta = \frac{C_0 - C}{C_0} \times 100\% \quad (1)$$

where C_0 is the absorbance of original MB solution and C is the absorbance of the MB solution after visible LED light irradiation.

According to the Langmuir–Hinshelwood kinetics model, the photocatalytic process of MB can be expressed as the following apparent pseudo-first-order kinetics equation [46]:

$$\ln \frac{C_0}{C} = k_{app}t \quad (2)$$

where k_{app} is the apparent pseudo-first-order rate constant, C_0 the original MB concentration and C is MB concentration in aqueous solution at time t .

3. Results and discussion

Fig. 3a–c shows the SEM images of F-TiO₂, g-C₃N₄ and 30%g-C₃N₄/F-TiO₂ hybrids. As indicated in Fig. 3a, the large amount of F-TiO₂ nanosheets with side length of 50–60 nm and thickness of 10–15 nm can be easily observed. The g-C₃N₄ shows the wrinkle two-dimensional structure in Fig. 3b. EDS in Fig. 3d shows the presence of F element on TiO₂ nanosheets. HRTEM image in Fig. 3h

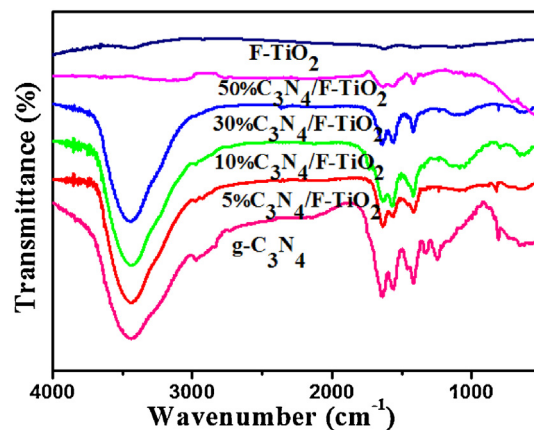


Fig. 5. FT-IR spectra of g-C₃N₄, F-TiO₂ and g-C₃N₄/F-TiO₂ hybrids.

shows the clear lattice fringes in g-C₃N₄/F-TiO₂ hybrids, a lattice plane separation of 0.325 nm that corresponds to the inter-layer structural packing, indexed for the (002) crystallographic plane of g-C₃N₄, it can be found that the F-TiO₂ lie on {002} facets of g-C₃N₄. On the other hand, HRTEM proved the top surface of F-TiO₂ is {001} facets. So, we can deem that the coupling between F-TiO₂ and g-C₃N₄ happened on F-TiO₂-{001} facets and g-C₃N₄-{002} facets.

Fig. 4 shows the XRD patterns of g-C₃N₄, F-TiO₂ and g-C₃N₄/F-TiO₂ hybrids. The very strong diffraction angles at $2\theta = 25.34^\circ$, 37.82° , 48.08° , 53.94° , 55.10° , 62.78° and 68.80° , can be assigned to (101), (004), (200), (105), (211), (204) and (116) crystal planes of pure TiO₂ with the anatase phase and the lines match well with the value reported by JCPDS (No. 21-1272, space group:

I41/amd (141), $a = 0.379$ nm and $c = 0.951$ nm). For pure g-C₃N₄, the strongest XRD peak at 27.3° , corresponding to 0.325 nm, was indexed as (002) diffraction plane (JCPDS 87-1526). When F-TiO₂ coupled with g-C₃N₄, it can be found that the (002) peak of g-C₃N₄ shifted to 27.8° , it implied that the coupling facets of g-C₃N₄ is g-C₃N₄-{002}[47], and this result is consistent with that of the HRTEM image.

Fig. 5 shows the FT-IR spectra of the g-C₃N₄, F-TiO₂ and g-C₃N₄/F-TiO₂ hybrids photocatalysts. In the case of pure g-C₃N₄, the broad peak at 3436 cm^{-1} may be due to the physically adsorbed water [48]. The strong bands at the $1200\text{--}1650\text{ cm}^{-1}$ region were found in the spectrum, the absorption band at 1640 cm^{-1} is attributed to C–N stretching, while the three at 1238 , 1322 and 1405 cm^{-1} to aromatic C–N stretching [49,50]. The band near

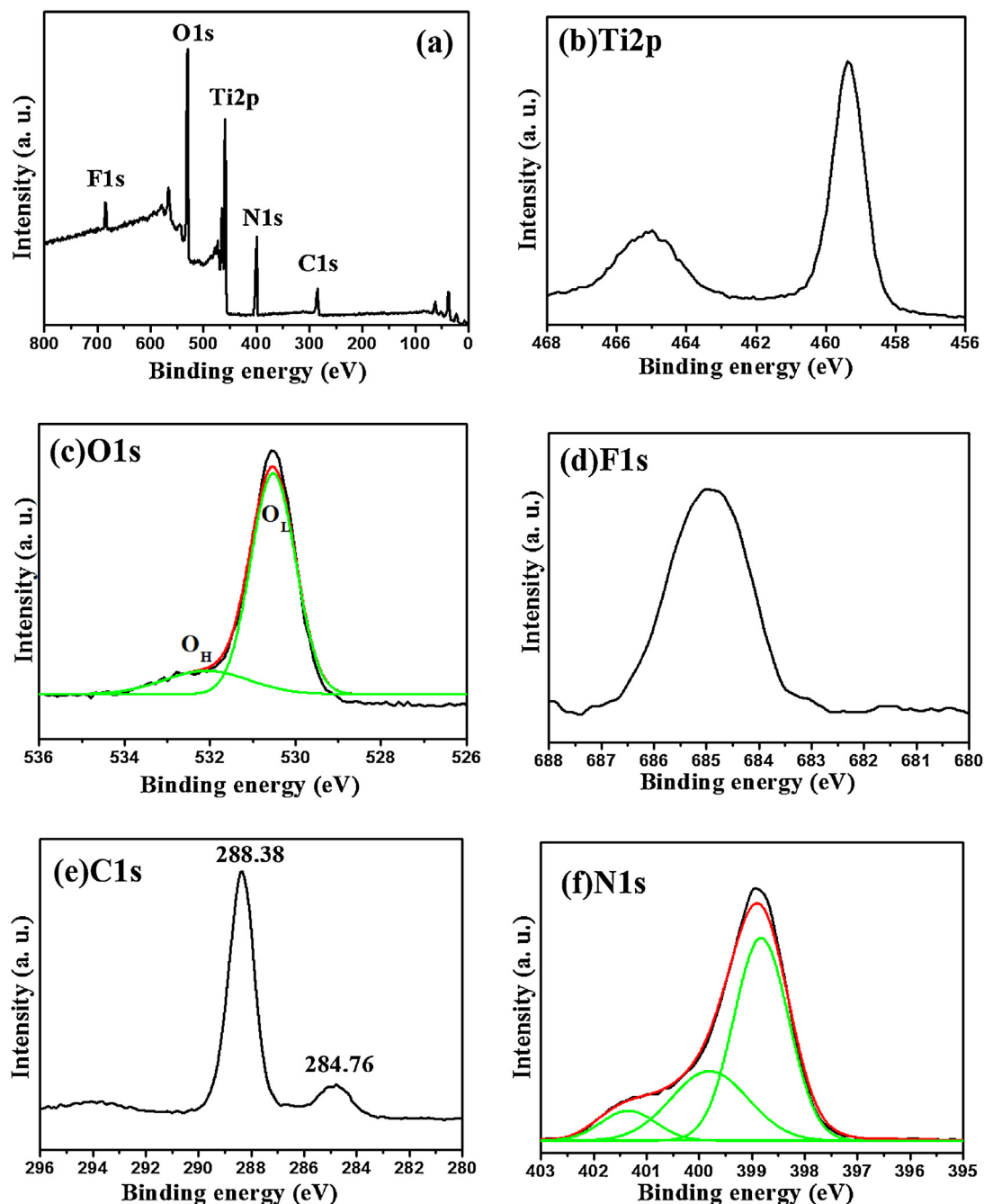


Fig. 6. The overview (a) and the corresponding high-resolution XPS spectra (b) C1s, (c) O1s, (d) Ti2p and (e) F1s of the as-prepared 30% C₃N₄/F-TiO₂.

809 cm⁻¹ is attributed to out-of plane bending modes of C–N heterocycles [51]. This result is consistent with that of the XRD experiment.

Fig. 6a shows the XPS spectrum including signals for C1s, Ti2p, O1s and F1s of 30%g-C₃N₄/F-TiO₂ nanosheets to probe the chemical environment of the elements in the near surface range. As indicated in Fig. 6b, the binding energies of Ti2p_{3/2} and 2p_{1/2} are centered at 459.37 and 465.04 eV, in agreement with those of pure TiO₂ [52]. Fig. 6c shows the high-resolution spectra of O1s. The curve fitting of O1s spectra basically indicates two components centered at 529.52 and 531.08 eV in 30%g-C₃N₄/F-TiO₂ hybrid are attributed to lattice oxygen and hydroxyl radicals [53], implying that oxygen vacancy and surface hydroxyl formed in the hybrid which are active species in semiconductor photocatalysis. Fig. 6d shows the F1s centered at 684.28 eV, typical feature peak for F-TiO₂ systems such as ≡Ti–F species on the F-TiO₂ crystal surface, and F species play an important role in the formation of oxygen vacancies and the fluorination on the surface of F-TiO₂ can accelerate the photocatalytic degradation of a wide range of organic pollutants since the •OH radicals generated on the surface of F-TiO₂ are more mobile than those generated on pure TiO₂ [54]. As indicated in Fig. 6e, the asymmetrical and broad features of the observed C1s peaks suggest the co-existence of distinguishable models. A deconvolution core level spectrum at about 284.76 and 288.38 eV has been presented. The major peak at 284.76 eV is exclusively assigned to carbon atoms (C–C bonding) in a pure carbon environment, i.e., graphitic or amorphous carbons either in our sample or adsorbed to the surface [55]. The peak at 288.38 eV is identified as originating from carbon atoms bonded to three nitrogen atoms in the g-C₃N₄ lattice [56]. The high resolution N1s XPS spectra in Fig. 6f shows an asymmetrical feature indicating the co-existence of a number of distinguishable nitrogen environments; fitting with three results in binding energies of 398.86, 399.80 and 401.36 eV. The two peaks at 399.80 and 401.36 eV can be assigned to tertiary nitrogen (N–(C)₃) and amino functional groups having a hydrogen atom (C–N–H) [57,58]. The peak at 398.86 eV is typically attributed to N atoms sp²-bonded to two carbon atoms (C=N–C) [59], thus confirming the presence of graphite-like sp²-bonded g-C₃N₄.

Fig. 7a shows the nitrogen adsorption–desorption isotherms for g-C₃N₄, F-TiO₂ and g-C₃N₄/F-TiO₂ hybrids at 77 K. Fig. 7b summarizes the BET surface area of g-C₃N₄/F-TiO₂ hybrids with different loading amounts of g-C₃N₄. It is found that pure F-TiO₂ nanosheets (89 m²/g) have a larger surface area than that of g-C₃N₄ (16 m²/g). When g-C₃N₄ is facet coupling with F-TiO₂ nanosheets, the surface area of g-C₃N₄/F-TiO₂ hybrids is decreased with the increased content of g-C₃N₄.

UV–vis DRS of the samples have been shown in Fig. 8. The fundamental absorption edge of anatase TiO₂ nanosheet is about 392 nm, whereas g-C₃N₄ exhibits absorption edge in 463 nm. The band gap energy of the prepared catalysts can be calculated by the following formula [60]:

$$\alpha h\nu \sim \frac{(h\nu - E_g)^{1/2}}{h\nu} \quad (3)$$

where α and E_g are the absorption coefficient and energy band gap (at wave vector $k=0$) of the semiconductor, respectively. According to Eq. (3), plots of $(\alpha h\nu)^2$ versus energy ($h\nu$) for photocatalysts are shown in Fig. 8b. From the tangent line of the curve, extrapolated to the $h\nu$ axis intercept, E_g of g-C₃N₄ and F-TiO₂ were estimated as 2.68 and 3.16 eV. With increasing g-C₃N₄ contents, the absorption edge of g-C₃N₄/F-TiO₂ hybrid has a clear mono tonic red shift meanwhile the absorption intensity of g-C₃N₄/F-TiO₂ hybrid is enhanced gradually.

In order to investigate the influence of the F-TiO₂, PL analysis was applied to investigate the separation efficiency of photogenerated electrons and holes in g-C₃N₄/F-TiO₂ samples. Fig. 9 shows

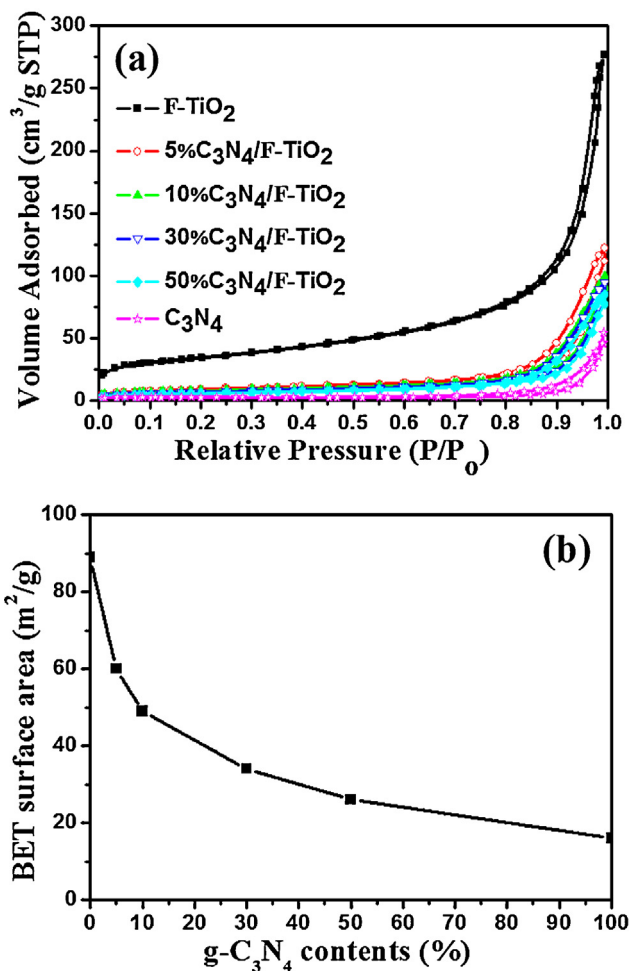


Fig. 7. (a) Isotherms for nitrogen adsorption–desorption and (b) BET surface area versus different g-C₃N₄ contents samples.

the PL spectra of the pure g-C₃N₄ and g-C₃N₄/F-TiO₂ hybrid materials excited by 325 nm. The main emission peak was centered at about 460 nm for the pure g-C₃N₄ sample, which was similar to the literatures [48]. For g-C₃N₄/F-TiO₂ hybrid materials, the position of the emission peak in the PL spectrum was similar to that of the pure g-C₃N₄, but the emission intensity significantly decreased, which indicated that the g-C₃N₄/F-TiO₂ composites had much lower recombination rate of photo-generated charge carriers. This demonstrated that the recombination of photogenerated charge carriers was greatly inhibited by the introduction of F-TiO₂, showing that the photogenerated electrons and holes in g-C₃N₄/F-TiO₂ hybrid materials had higher separation efficiency than those in the pure g-C₃N₄, consistent with the photocurrent and photocatalytic testing results.

Presently, the photocurrent is widely regarded as the most efficient evidence for demonstrating the electrons and holes separation in the composite photocatalysts [61,62]. A relationship is commonly recognized as follows: the higher the photocurrent, the higher the electrons–holes separation efficiency, and thus, the higher the photocatalytic activity. To give further evidence to support the mechanism suggested above, photocurrent–time measurements were performed for a 350 s period under 410 nm LED light illumination in an on-and-off cycle mode. Fig. 10 shows the photocurrent–time curves of Degussa P25, g-C₃N₄, F-TiO₂, and the g-C₃N₄/F-TiO₂ hybrid with two on–off intermittent irradiation cycles. The electrodes of the samples demonstrate a rapid photocurrent response when the LED light illumination is on an

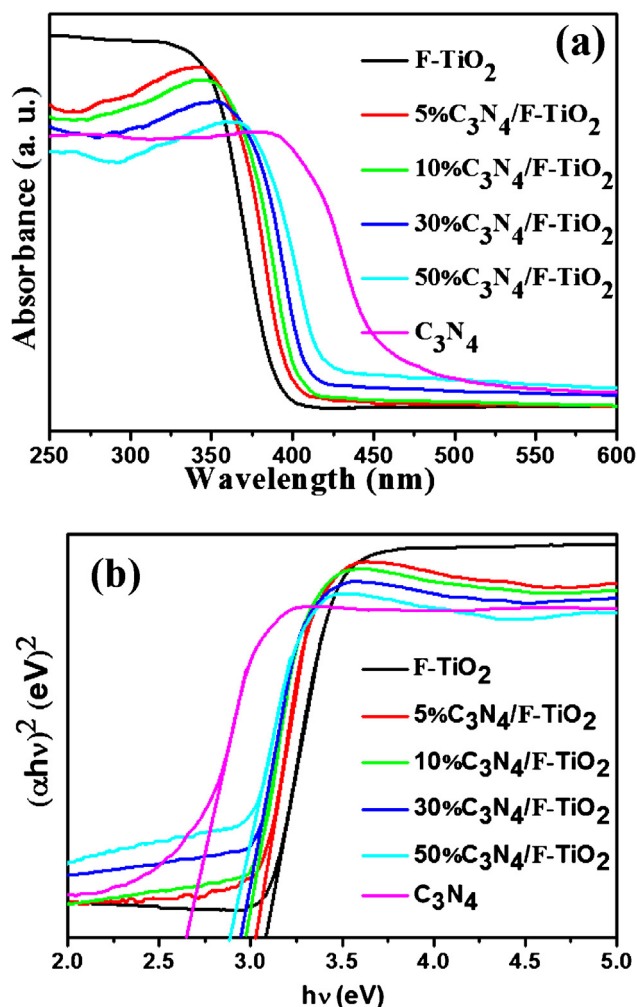


Fig. 8. (a) UV-vis DRS spectra and (b) plots of $(\alpha h\nu)^2$ versus energy ($h\nu$) for pure TiO₂, g-C₃N₄ and g-C₃N₄/F-TiO₂ hybrids.

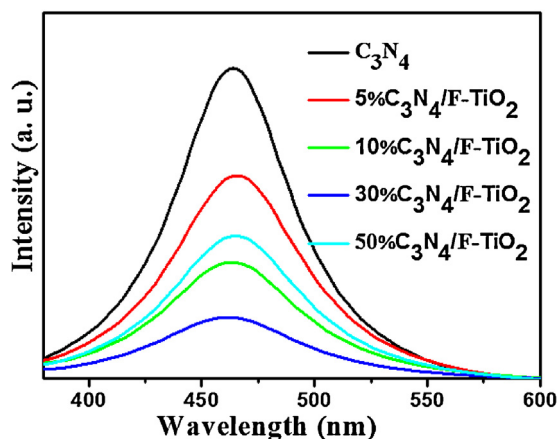


Fig. 9. Comparison of PL spectra of pure g-C₃N₄ and g-C₃N₄/F-TiO₂ hybrid samples.

on-and-off mode. The 30%g-C₃N₄/F-TiO₂ presents the highest photocurrent intensity, thus the 30%g-C₃N₄/F-TiO₂ hybrid has the lowest electrons and holes recombination rate.

Fig. 11a shows the MB adsorption on Degussa P25, F-TiO₂, g-C₃N₄ and g-C₃N₄/F-TiO₂ hybrid in the dark. F-TiO₂ shows the highest adsorption capacity because of its highest specific surface area. The photocatalytic activity of g-C₃N₄/F-TiO₂ photocatalysts

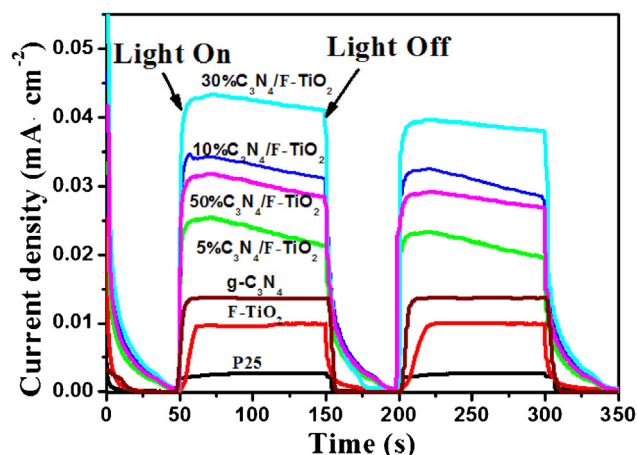


Fig. 10. Transient photocurrent responses of Degussa P25, F-TiO₂, g-C₃N₄ and g-C₃N₄/F-TiO₂ hybrid.

was studied by degradation of MB under 410 nm LED light irradiation sources. As a comparison, MB degradation with pure TiO₂, Degussa P25 and no catalyst was also carried out under identical conditions. As shown in Fig. 11b, the degradation of MB in Degussa P25, TiO₂, 5%g-C₃N₄/F-TiO₂, 10%g-C₃N₄/F-TiO₂, 30%g-C₃N₄/F-TiO₂, 50%g-C₃N₄/F-TiO₂ and g-C₃N₄ was 15%, 34%, 59%, 71%, 89%, 61% and 42%, respectively. According to Fig. 11a and b, the absorption of MB on all these materials is not a major factor that obviously influence their photocatalytic performance. Fig. 11c shows that there is a linear relationship between $\ln C_0/C$ and t , confirming that the photodegradation reaction is indeed pseudo-first-order. According to Eq. (2) and Fig. 11c and d shows the apparent pseudo-first-order rate constant k_{app} with different catalysts. k_{app} of the photodegradation of MB are 0.0027, 0.0083, 0.0166, 0.0230, 0.0374, 0.0184, 0.0096 min⁻¹ for Degussa P25, TiO₂, 5%g-C₃N₄/F-TiO₂, 10%g-C₃N₄/F-TiO₂, 30%g-C₃N₄/F-TiO₂, 50%g-C₃N₄/F-TiO₂ and g-C₃N₄, respectively. An optimal degradation performance of 89% MB was found for 30%g-C₃N₄/F-TiO₂, 30%g-C₃N₄/F-TiO₂ showing superior catalytic activity to commercial Degussa P25, pure TiO₂ and other g-C₃N₄/F-TiO₂ hybrids.

It was well known that the enhancement of photocatalytic performance of composite photocatalysts was mainly attributed to electrons and holes transfer at the interfaces of photocatalysts. When F-TiO₂-{001} facets coupled with g-C₃N₄-{002} facets, the band edge potential position of the g-C₃N₄ and g-C₃N₄/F-TiO₂ hybrid materials played an important role in studying the efficient generation and separation process of the electrons and holes pairs. The valence band (VB) potentials of a semiconductor at the point of zero charge can be theoretically predicted by the following empirical equation [63]:

$$E_{VB} = X - E^c + 0.5E_g \quad (4)$$

where E_{VB} is the VB edge potential, X the electronegativity of the semiconductor, which is the geometric mean of the electronegativity of the constituent atoms, E^c the energy of free electrons on the hydrogen scale (about 4.5 eV), E_g is the band gap energy of the semiconductor. Moreover, the conduction band (CB) edge potential (E_{CB}) can be obtained by $E_{CB} = E_{VB} - E_g$. The E_g of g-C₃N₄ and F-TiO₂ were estimated as 2.68 and 3.16 eV. The X values for the g-C₃N₄ and TiO₂ materials are 4.72 and 5.81 eV, respectively. Herein, the CB and VB edge potentials of g-C₃N₄ were determined at -1.12 and +1.56 eV, respectively. The CB and VB edge potentials of TiO₂ were calculated at -0.27 and +2.89 eV, respectively. Since the CB edge potential of g-C₃N₄ (-1.12 eV) is more negative than that of TiO₂ (-0.27 eV) the photoinduced electrons on g-C₃N₄ particle surfaces

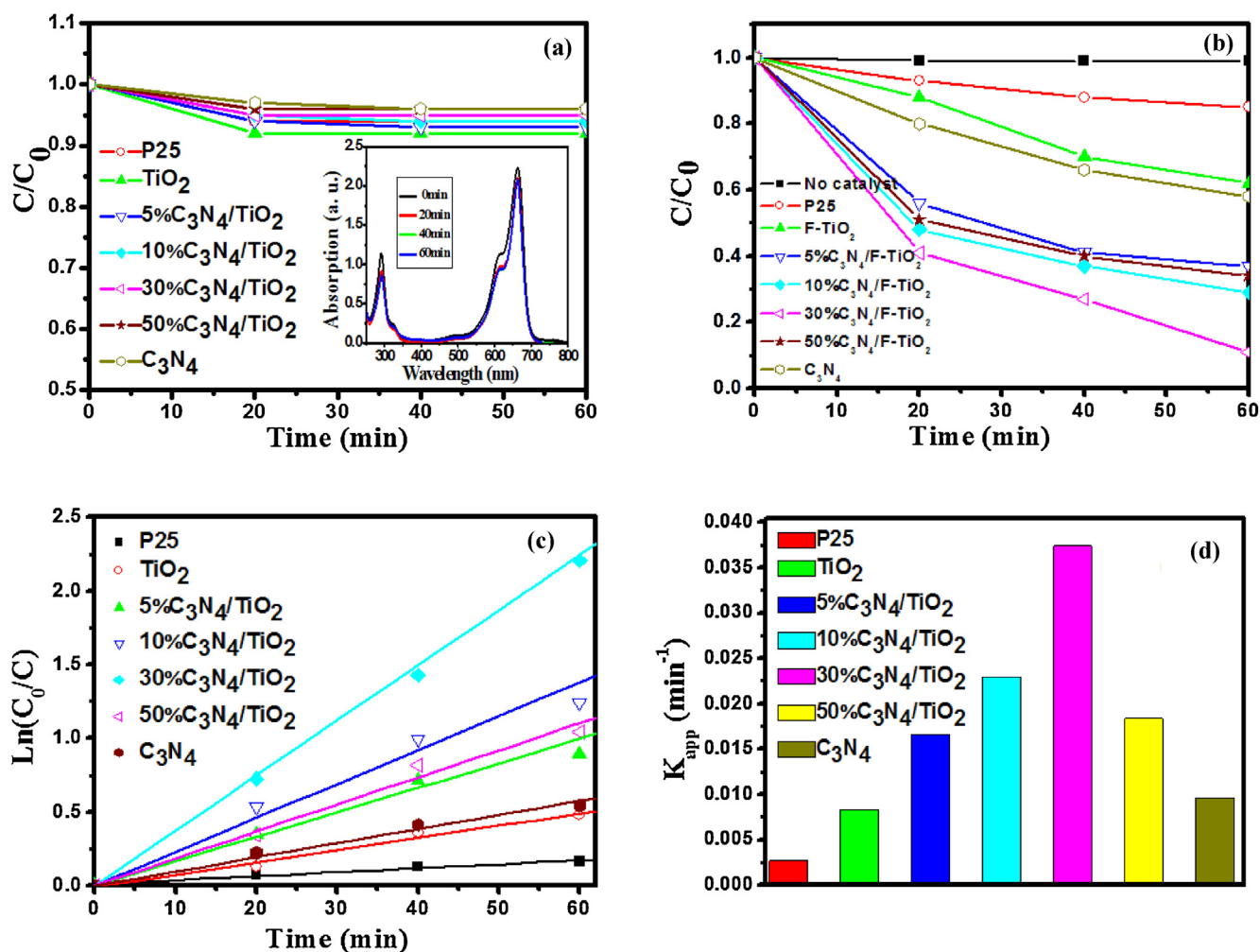


Fig. 11. (a) MB adsorption on Degussa P25, F-TiO₂, g-C₃N₄ and g-C₃N₄/F-TiO₂ hybrid in the dark (Inset: Absorption spectra of MB in the presence of 30%g-C₃N₄/F-TiO₂ composite), (b) photocatalytic degradation of MB under 410 nm LED light irradiation, (c) linear transform $\ln(C_0/C)$ of the kinetic curves of MB degradation, (d) the apparent pseudo-first-order rate constant k_{app} with different catalysts.

transfer easily to TiO₂ via the well developed interface. However, the photo-induced holes were suspended in g-C₃N₄ due to the large difference in VB edge potentials and oxidize the MB to H₂O, CO₂ and other inorganic molecule.

Based on the above information, the band structure diagram of g-C₃N₄/F-TiO₂ hybrids and the possible charge separation

processes is shown in Fig. 12. For the single semiconductor photocatalyst, g-C₃N₄ semiconductor can be excited under 410 nm LED light irradiation (energy less than 3.02 eV) and induce the generation of electrons and holes. However, electrons and holes recombined rapidly because of the narrow energy gap and big sizes. While F-TiO₂ cannot be activated under 410 nm light irradiation.

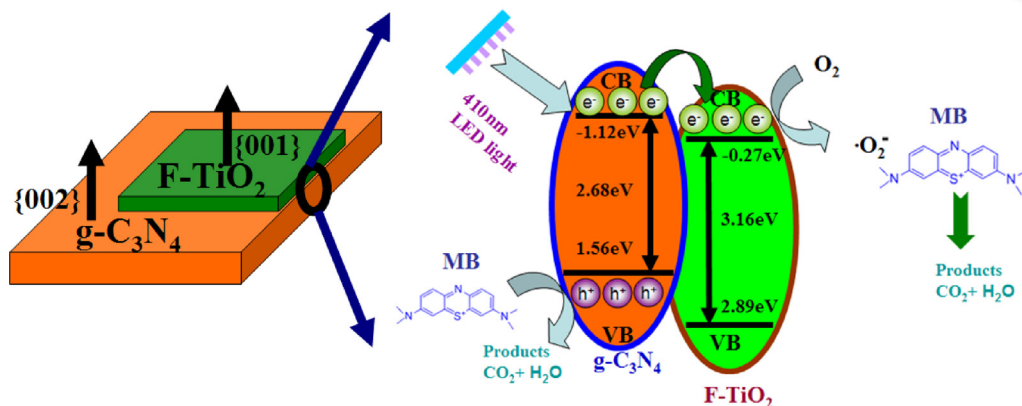


Fig. 12. A proposed visible LED light photodegradation mechanism of g-C₃N₄/F-TiO₂ hybrid photocatalyst.

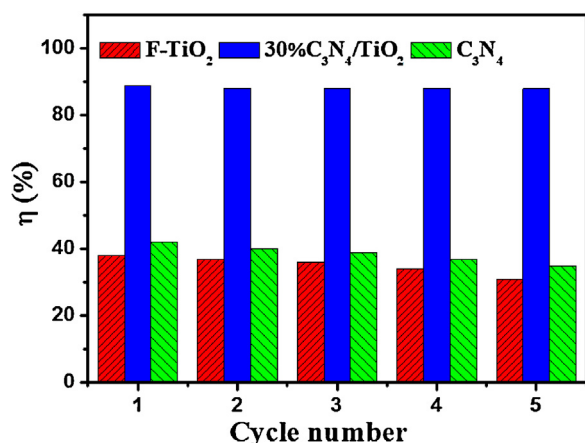
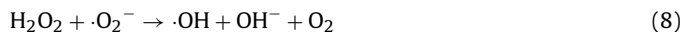
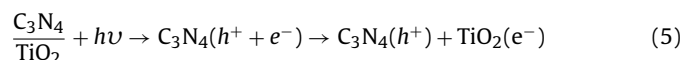


Fig. 13. Comparison of photodegradation performance within five cycles for 30%g-C₃N₄/F-TiO₂, g-C₃N₄ and F-TiO₂.

As can be seen from Fig. 12, when g-C₃N₄/F-TiO₂ hybrid was used as the photocatalyst, g-C₃N₄ could absorb the visible light, photoinduced electrons on the g-C₃N₄ surface can migrate easily to the CB of F-TiO₂, leaving holes on the g-C₃N₄ valence band. By this way, electrons and holes pairs could be effectively separated. Therefore, the efficient photocatalytic degradation of MB can smoothly proceed. The process is described as follows:



As a result, the photocatalytic activity of g-C₃N₄/F-TiO₂ hybrid is much higher than that of pure g-C₃N₄ or F-TiO₂. However, with the content of g-C₃N₄ in g-C₃N₄/F-TiO₂ hybrid being in excess, numerous photoinduced electrons and holes would recombine easily on the surface of g-C₃N₄ as mentioned above. Therefore, 30%g-C₃N₄ hybrid exhibited the best photocatalytic activity among these different g-C₃N₄/F-TiO₂ photocatalysts.

Stability of the photocatalyst is crucially important for practical applications. To evaluate the stability of g-C₃N₄/TiO₂ hybrids, we carried out the recycle experiment under identical conditions. As shown in Fig. 13, the photocatalytic activity of the as-prepared 30%g-C₃N₄/TiO₂ hybrids photocatalyst still maintains a high level even after 5 times cycling.

4. Conclusions

In summary, nanosheet/nanosheet heterojunctions structural hybrid of F-TiO₂ and g-C₃N₄ exhibit largely reduced PL intensity than the solely components, indicating effectively depressed recombination of electron and holes due to the effective formation of planar heterojunctions. The photoelectrochemical current measurement has shown largely increased photocurrent that is composed of un-recombined photogenerated electrons and holes. In the photocatalytic experiment, the hybrid displayed improved MB photodegradation activity under visible light irradiation comparing with pure F-TiO₂ and g-C₃N₄. An optimal degradation performance was found for 30%g-C₃N₄/F-TiO₂, which is 13.9 times than that of commercial Degussa P25 TiO₂. The structure

engineering of heterojunction photocatalysts is of great value for designing advanced photocatalyst.

Acknowledgments

This work was supported by the National Natural Science Foundation of China (51302101, 21303129, 11004071), the Natural Science Foundation of Anhui Province (1408085QE78), the key Foundation of Educational Commission of Anhui Province (KJ2012A250) and the Huaibei Science and Technology Development Funds (20110305).

References

- [1] M.A. Shannon, P.W. Bohn, M. Elimelech, J.G. Georgiadis, B.J. Marinas, A.M. Mayes, *Nature* 452 (2008) 301–310.
- [2] L. Jing, W. Zhou, G. Tian, H. Fu, *Chem. Soc. Rev.* 42 (2013) 9509–9549.
- [3] F.E. Osterloh, *Chem. Soc. Rev.* 42 (2013) 2294–2320.
- [4] N. Serpone, A.V. Emeline, *J. Phys. Chem. Lett.* 3 (2012) 673–677.
- [5] X. Lang, X. Chen, J. Zhao, *Chem. Soc. Rev.* 43 (2014) 473–486.
- [6] H. Tong, S. Ouyang, Y. Bi, N. Umezawa, M. Oshikiri, J. Ye, *Adv. Mater.* 24 (2012) 229–251.
- [7] Q. Xiang, J. Yu, M. Jaroniec, *Chem. Soc. Rev.* 41 (2012) 782–796.
- [8] K. Dai, L. Lu, J. Dong, Z. Ji, G. Zhu, Q. Liu, Z. Liu, Y. Zhang, D. Li, C. Liang, *Dalton Trans.* 42 (2013) 4657–4662.
- [9] G. Xi, J. Ye, Q. Ma, N. Su, H. Bai, C. Wang, *J. Am. Chem. Soc.* 134 (2012) 6508–6511.
- [10] Y. Bi, S. Ouyang, N. Umezawa, J. Cao, J. Ye, *J. Am. Chem. Soc.* 133 (2011) 6490–6492.
- [11] G. Jiang, R. Wang, X. Wang, X. Xi, R. Hu, Y. Zhou, S. Wang, T. Wang, W. Chen, *ACS Appl. Mater. Interfaces* 4 (2012) 4440–4444.
- [12] W.C. Huang, L.M. Lyu, Y.C. Yang, M.H. Huang, *J. Am. Chem. Soc.* 134 (2012) 1261–1267.
- [13] X. Chen, S.S. Mao, *Chem. Rev.* 107 (2007) 2891–2959.
- [14] Y. Wang, H. Sun, S. Tan, H. Feng, Z. Cheng, J. Zhao, A. Zhao, B. Wang, Y. Luo, J. Yang, J.G. Hou, *Nat. Commun.* 4 (2013) 2214.
- [15] X. Chen, L. Liu, P.Y. Yu, S.S. Mao, *Science* 331 (2011) 746–750.
- [16] Y. Yin, A.P. Alivisatos, *Nature* 437 (2005) 664–670.
- [17] U. Diebold, *Surf. Sci. Rep.* 48 (2003) 53–229.
- [18] H. Yang, C. Sun, S. Qiao, J. Zou, G. Liu, S.C. Smith, H.M. Cheng, G.Q. Lu, *Nature* 453 (2008) 638–641.
- [19] Y. Dai, C.M. Cobley, J. Zeng, Y. Sun, Y. Xia, *Nano Lett.* 9 (2009) 2455–2459.
- [20] L. Etgar, W. Zhang, S. Gabriel, S.G. Hickey, M.K. Nazeeruddin, A. Eychmüller, B. Liu, M. Grätzel, *Adv. Mater.* 24 (2012) 2202–2206.
- [21] Q. Xiang, J. Yu, M. Jaroniec, *J. Am. Chem. Soc.* 134 (2012) 6575–6578.
- [22] X. Luo, F. Deng, L. Min, S. Luo, B. Guo, G. Zeng, C. Au, *Environ. Sci. Technol.* 47 (2013) 7404–7412.
- [23] J. Matos, E. García-López, L. Palmisano, A. García, G. Marci, *Appl. Catal. B: Environ.* 99 (2010) 170–180.
- [24] Z. Zhang, C. Shao, X. Li, Y. Sun, M. Zhang, J. Mu, P. Zhang, Z. Guo, Y. Liu, *Nanoscale* 5 (2013) 606–618.
- [25] Y. Yu, M.-Z. Zhang, J. Chen, Y.-D. Zhao, *Dalton Trans.* 42 (2013) 885–889.
- [26] C. An, W. Jiang, J. Wang, S. Wang, Z. Ma, Y. Li, *Dalton Trans.* 42 (2013) 8796–8801.
- [27] Y. Lin, Y. Li, X. Zhan, *Chem. Soc. Rev.* 41 (2012) 4245–4272.
- [28] J. Su, L. Guo, N. Bao, C.A. Grimes, *Nano Lett.* 11 (2011) 1928–1933.
- [29] Q. Xu, F. Wang, D. Qian, Z. Tan, L. Li, S. Li, X. Tu, G. Sun, X. Hou, Y. Li, *ACS Appl. Mater. Interfaces* 5 (2013) 6591–6597.
- [30] S.G. Kumar, K.S.R.K. Rao, *Energy Environ. Sci.* 7 (2014) 45–102.
- [31] K. Dai, L. Lu, Q. Liu, G. Zhu, Q. Liu, Z. Liu, *Dalton Trans.* 43 (2014) 2202–2210.
- [32] X. Bai, R. Zong, C. Li, D. Liu, Y. Liu, Y. Zhu, *Appl. Catal. B: Environ.* 147 (2014) 82–91.
- [33] X. Bai, L. Wang, R. Zong, Y. Zhu, *J. Phys. Chem. C* 117 (2013) 9952–9961.
- [34] X. Wang, S. Blechert, M. Antonietti, *ACS Catal.* 2 (2012) 1596–1606.
- [35] Y. Zheng, J. Liu, J. Liang, M. Jaroniec, S.Z. Qiao, *Energy Environ. Sci.* 5 (2012) 6717–6731.
- [36] X.-H. Li, M. Antonietti, *Chem. Soc. Rev.* 42 (2013) 6593–6604.
- [37] Y. Sun, S. Gao, Y. Xie, *Chem. Soc. Rev.* 43 (2014) 530–546.
- [38] X.C. Wang, K. Maeda, A. Thomas, K. Takanabe, G. Xin, J.M. Carlsson, K. Domen, M. Antonietti, *Nat. Mater.* 8 (2009) 76–80.
- [39] S.C. Yan, Z.S. Li, Z.G. Zou, *Langmuir* 25 (2009) 10397–10401.
- [40] Y. Wang, R. Shi, J. Lin, Y. Zhu, *Energy Environ. Sci.* 4 (2011) 2922–2929.
- [41] L. Sun, X. Zhao, C.J. Jia, Y. Zhou, X. Cheng, P. Li, L. Liu, W. Fan, *J. Mater. Chem.* 22 (2012) 23428–23438.
- [42] H. Xu, J. Yan, Y. Xu, Y. Song, H. Li, J. Xia, C. Huang, H. Wan, *Appl. Catal. B: Environ.* 129 (2013) 182–193.
- [43] T. Li, L. Zhao, Y. He, J. Cai, M. Luo, J. Lin, *Appl. Catal. B: Environ.* 129 (2013) 255–263.
- [44] L. Ge, C. Han, J. Liu, *Appl. Catal. B: Environ.* 108–109 (2011) 100–107.
- [45] L. Huang, H. Xu, Y. Li, H. Li, X. Cheng, J. Xi, Y. Xu, G. Cai, *Dalton Trans.* 42 (2013) 8606–8616.
- [46] K. Dai, L. Lu, Q. Liu, G. Zhu, Q. Liu, *Catal. Commun.* 43 (2014) 202–206.
- [47] L. Ye, J. Liu, Z. Jiang, T. Peng, L. Zan, *Appl. Catal. B: Environ.* 142–143 (2013) 1–7.

- [48] G. Liao, S. Chen, X. Quan, H. Yu, H. Zhao, *J. Mater. Chem.* 22 (2012) 2721–2726.
- [49] Y. Bu, Z. Chen, J. Yu, W. Li, *Electrochim. Acta* 88 (2013) 294–300.
- [50] Y. Wang, X. Bai, C. Pan, J. He, Y. Zhu, *J. Mater. Chem.* 22 (2012) 11568–11573.
- [51] F. Dong, L. Wu, Y. Sun, M. Fu, Z. Wu, S.C. Lee, *J. Mater. Chem.* 21 (2011) 15171–15174.
- [52] B.M. Reddy, B. Chowdhury, P.G. Smirniotis, *Appl. Catal. A Gen.* 211 (2001) 19–30.
- [53] J.G. Yu, H.G. Yu, B. Cheng, X.J. Zhao, J.C. Yu, W.K. Ho, *J. Phys. Chem. B* 107 (2003) 13871–13879.
- [54] T.R. Gordon, M. Cargnello, T. Paik, F. Mangolini, R.T. Weber, P. Fornasiero, C.B. Murray, *J. Am. Chem. Soc.* 134 (2012) 6751–6761.
- [55] A.P. Dementjev, A. de Graaf, M.C.M. van de Sanden, K.I. Maslakov, A.V. Naumkin, A.A. Serov, *Diamond Relat. Mater.* 9 (2000) 1904–1907.
- [56] Y. Cui, J. Zhang, G. Zhang, J. Huang, P. Liu, M. Antonietti, X. Wang, *J. Mater. Chem.* 21 (2011) 13032–13039.
- [57] S.H. Bian, Z. Ma, W.G. Song, *J. Phys. Chem. C* 113 (2009) 8668–8672.
- [58] C. Miranda, H. Mansilla, J. Yáñez, S. Obregón, G. Colón, *J. Photochem. Photobiol. A: Chem.* 253 (2013) 16–21.
- [59] L. Ge, C. Han, J. Liu, *J. Mater. Chem.* 22 (2012) 11843–11850.
- [60] X. Wang, K. Maeda, A. Thomas, K. Takanabe, G. Xin, J.M. Carlsson, K. Domen, M. Antonietti, *Nat. Mater.* 8 (2009) 76–80.
- [61] Y. Lin, S. Zhou, X. Liu, S. Sheehan, D. Wang, *J. Am. Chem. Soc.* 131 (2009) 2772–2773.
- [62] P.V. Kamat, *J. Phys. Chem. C* 112 (2008) 18737–18753.
- [63] X. Zhang, L.Z. Zhang, T.F. Xie, D.J. Wang, *J. Phys. Chem. C* 113 (2009) 7371–7378.